

Towards High-accuracy and Low-latency Spiking Neural Networks with Two-Stage Optimization

Ziming Wang, Yuhao Zhang, Shuang Lian, Xiaoxin Cui, *Member, IEEE*, Rui Yan, *Member, IEEE*, and *Huajin Tang, *Senior Member, IEEE*

Abstract—Spiking neural networks (SNNs) operating with asynchronous discrete events show higher energy efficiency with sparse computation. A popular approach for implementing deep SNNs is ANN-SNN conversion combining both efficient training of ANNs and efficient inference of SNNs. However, the accuracy loss is usually non-negligible, especially under few time steps, which restricts the applications of SNN on latency-sensitive edge devices greatly. In this paper, we first identify that such performance degradation stems from the misrepresentation of the negative or overflow residual membrane potential in SNNs. Inspired by this, we decompose the conversion error into three parts: quantization error, clipping error, and residual membrane potential representation error. With such insights, we propose a two-stage conversion algorithm to minimize those errors respectively. Besides, We show each stage achieves significant performance gains in a complementary manner. By evaluating on challenging datasets including CIFAR-10, CIFAR-100 and ImageNet, the proposed method demonstrates the state-of-the-art performance in terms of accuracy, latency and energy preservation. Furthermore, our method is evaluated using a more challenging object detection task, revealing notable gains in regression performance under ultra-low latency when compared to existing spike-based detection algorithms. Codes are available at <https://github.com/Windere/snn-cvt-dual-phase>.

Index Terms—ANN-SNN Conversion, two-stage optimization, spiking neural network (SNN), deep SNNs, residual membrane potential, spike-based object detection, neuromorphic computing

I. INTRODUCTION

SPIKING neural networks (SNNs), inspired by mimicking the dynamics of biological neurons [1]–[3], have gained increasing interest [4]. Different from the computation with single, continuous-valued activation in ANNs, SNNs use binary spikes to transmit and process information. Each neuron in the SNNs will remain silent without energy consumption until receiving a spike/event afferent [5]. Such an event-driven

computing paradigm enables more power-efficient solutions on dedicated neuromorphic hardware by substituting dense multiplication with sparse addition [6]. As reported in [7]–[9], SNNs on specified neuromorphic processors can achieve orders of magnitude lower energy consumption and latency compared with ANNs. In addition, SNNs could synergistically help denoise redundant information with inherent temporal dynamics [10]. However, it is still an open problem how to obtain highly-performance SNNs efficiently.

In general, there are two mainstream methodologies for developing supervised deep SNNs up to date: (1) direct training for SNNs and (2) converting ANNs into SNNs. For direct training methods, the back-propagation technique could not be applied to SNNs directly due to the threshold-crossing firing in spiking neurons, which presents challenges for accurately calculating gradients in both spatial and temporal domains. Some researchers have suggested to circumvent this difficulty by designing a surrogate function and smoothing the non-differentiable spike firing [11]–[15]. To efficiently utilize the temporal structure in spike trains, the time-based scheme is proposed to directly assign credits to the shift of spike time in SNNs while taking both inter-neuron and intra-neuron dependencies [16]–[21] into account. Binary probabilistic models [22], [23] utilize stochasticity (e.g. the log-likelihood of a spike) to approximate the expectation value of gradients in SNNs. Dedicated to improving the performance, transfer learning in SNNs is also explored through transplanting features [24] or mitigating domain shift [25]. Nevertheless, it is still hard to train large-scale SNNs due to the limited memory capacity, the short-time dependency, and the vanishing spike rate in deep networks. Moreover, training SNNs on GPUs invariably incurs additional computational and memory overhead, which scales proportionally with the time step [26], as there is no specific optimization for storage and operations with binary events.

The alternative approach, known as ANN-SNN conversion, involves obtaining SNNs from pretrained ANNs, which has resulted in some best-performing SNNs on large-scale datasets like ImageNet [27] with significantly lower training costs compared to direct training. The core idea of conversion is to establish the consistent relationship between activations of analog neurons and some kind of aggregate representation of spiking neurons, such as spike count [28], spike rate [29], [30], and postsynaptic potential (PSP) [31]. With such clear criteria, ANN-SNN conversion has been applied to complex scenarios with competitive performances compared to ANNs [32]–[35]. Nevertheless, to achieve enough representation precision,

This work was supported by the National Natural Science Foundation of China under Grant 62236007.

Ziming Wang and Shuang Lian are with the College of Computer Science and Technology, Zhejiang University, Hangzhou 310027, China (e-mail: zi_ming_wang@zju.edu.com, slian@zju.edu.cn)

Yuhao Zhang is with the Research Center for Intelligent Computing Hardware, Zhejiang Lab, Hangzhou 311100, China (e-mail: zhangyuhao@zhejianglab.com)

Xiaoxin Cui is with the School of Integrated Circuits, Peking University, Beijing 100871, China (e-mail: cuixx@pku.edu.cn)

Rui Yan is with the College of Computer Science, Zhejiang University of Technology, Hangzhou 310014, China (e-mail: Ryan@zjut.edu.cn).

Huajin Tang (Corresponding author) is with the College of Computer Science and Technology and the State Key Laboratory of Brain-Machine Intelligence, Zhejiang University, Hangzhou 310027, China. (e-mail: htang@zju.edu.cn).

considerable simulation steps are usually required for nearly lossless conversion, known as the accuracy-delay tradeoff. It restricts the practical application of SNNs greatly. A large body of recent work [26], [36]–[38] proposes to alleviate this problem by exploiting the quantization and clipping properties of aggregation representations. Even though, there is still a significant performance gap between ANNs and SNNs under low inference latency (≤ 16 time steps). Some recent works have further bridged this performance gap by introducing a signed neuron model with a customized spike counter [39] or a neuron model firing burst spikes in a single time step [40], [41]. However, the underlying cause of performance degradation when mapping ANNs into SNNs is still unclear. Therefore, our focus is on analyzing conversion errors and improving the accuracy-delay tradeoff based on vanilla spiking neurons.

In this paper, we explicitly identify that the conversion error under few time steps primarily arises from the misrepresentation of the residual membrane potential, which can accurately characterizes information loss between the input and output of spiking neurons with asynchronous spike firing. Furthermore, we demonstrate that the error regarding residual potential representation is complementary to quantization and clipping errors. Inspired by this, we propose an ANN-SNN conversion algorithm with a two-stage optimization approach to mitigate these three types of errors. This approach achieves remarkable performance with extremely low inference delay. The main contributions of this work are summarized as follows:

- 1) We analyze the operator consistency between ANNs and SNNs theoretically and identify the neglected residual potential representation problem. Then we divide conversion errors into three parts: quantization error, clipping error, and residual potential representation error.
- 2) We propose a two-stage scheme for the threefold errors toward lossless conversion under ultra-low inference delay. In the first stage, quantization-clipping functions with trainable thresholds and quantization noise are applied to finetune ANNs. In the second stage, we minimize the residual potential error with layer-wise calibrations on weights and initial membrane potential. Additionally, we further extend it into ANNs with Leaky ReLU as activation.
- 3) Experimental results on the both CIFAR and ImageNet datasets show significant improvements in accuracy-latency tradeoffs compared to state-of-the-art methods across diverse architectures, including ResNet, VGG, ResNeXt, and MobileNet. For example, we achieved 70.13% top-1 accuracy (19.16% improvements) on ImageNet with VGG-16 under only 16 time steps.
- 4) A spike-based object detection model is implemented based on the proposed method. The results on the PASCAL VOC dataset demonstrate competitive detection performance with at least $25\times$ inference speedup in comparison to existing spike-based object detectors.

II. RELATED WORK

Cao *et al.* [42] first proposed to convert pretrained ANNs into SNNs and suggested the criterion of matching ANN

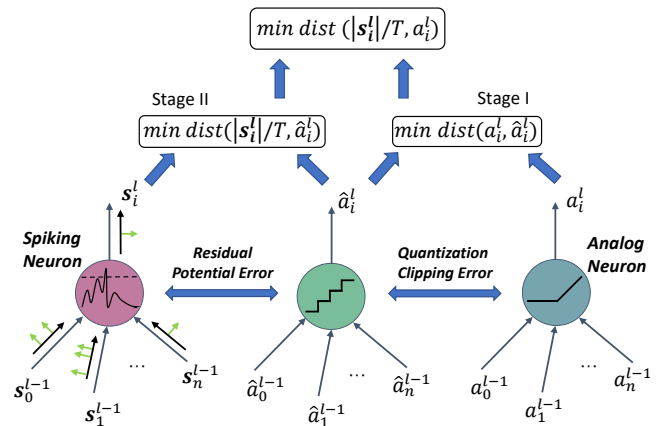


Fig. 1. The criterion of conversion in this article is to minimize the distance of spike rates $r_i^l = |s_i^l|/T$ and ANN activations a_i^l by minimizing three errors with two-stage methods at each layer. Here, $|s_i^l|$ represents the cardinal number of spike train s_i^l .

activation and spiking rate of SNN. After the launch of ANN-SNN conversion, the development of conversion algorithms could be divided into two routes in general.

From the perspective of constrained ANNs: Diehl *et al.* [29] found the importance of weight-threshold balance and design weight normalization based on the maximum of layer-wise ANN activations. Afterward, a lot of work was dedicated to developing more elaborate normalization factors such as robust normalization [30], spike-based normalization [43], channel-wise normalization [32], threshold-balancing [44], and normalization on shortcut connections [45]. These methods can be sufficiently integrated with ReLU-based ANN to achieve lossless conversion. However, the inference delay is up to hundreds or thousands in general. Exploring the characteristics of quantization and clipping in spike rate, Yan *et al.* [36] first proposed the training scheme with quantization and clipping constraints for ANNs, namely CQ-training. Similarly, Ding *et al.* [46] proposed the method for weight and threshold training by stages to optimize the upper bound of the error between ReLU and CQ activations. Ho *et al.* [38] suggested a trainable clipping bound in activation functions to balance the threshold. Recently, Bu *et al.* [37] approximated the activation of SNNs through a quantization clip-floor-shift function and explored the conversion error when the quantization step in ANNs and the time step in SNNs are mismatched. In addition to the conversion of full-precision weights, Wang *et al.* [47] further explored the high-performance conversion under binary weights by rectifying normalization coefficients.

From the perspective of modified SNNs: The soft reset mechanism is widely adopted [6], [42] to avoid information loss from potential reset. Deng *et al.* [31] decomposed the network conversion error into the layer-wise conversion error and proposed the extra shift of $\theta/(2T)$ in spiking neurons to reduce the expectation of quantization error. Comparably, Hu *et al.* [45] and Bu *et al.* [48] configured the initial membrane potential of spiking neurons as $\theta/2$ to reduce quantization error. Furthermore, Li *et al.* [26] exploited the calibration effect of a handful of samples through activation transplating

to reduce clipping error and quantization error. Yu *et al.* [40] first show the performance of SNNs could be enhanced greatly with augmented spike and double-threshold schemes. Wang *et al.* [39] introduced a signed neuron model with a specific spike counter to compensate for the inconsistency between synchronous ANNs and asynchronous SNNs. Li *et al.* [39] enhanced spiking neurons by allowing bursting spikes in a single time step, reducing the information loss. In addition to rate coding, customized neuron models [49], [50] based on temporal coding were also investigated further to exploit the temporal dynamics of spiking neurons. The work introduced by Hwang *et al.* [51] reduced inference latency by sequentially searching for the optimal initial membrane potential. By modulating the membrane potential towards a steady firing state of spiking neurons, those methods implicitly alleviate the representation problem from residual potential. However, without explicitly identifying and formulating the error function from residual potential, it is challenging to design targeted optimization strategies.

Different from previous approaches, this work is the first to explicitly identify the source of error responsible for the stable firing state, called the residual potential error (RPE). Furthermore, we have introduced an additional fine-tuning stage that is specifically designed to minimize this particular source of error, thereby enabling high-performance converted SNNs with ultra-low latency.

III. PRELIMINARIES

a) Analog Neuron Model: Analog neurons in feedforward neural networks, such as CNN and MLPs, communicate and learn with continuous activations. Mathematically, the forward computation of the l -th layer in feedforward networks is formed as:

$$a_i^l = \sigma(z_i^l) = \sigma\left(\sum_j W_{ij}^l \cdot a_j^{l-1} + b_i^l\right) \quad (1)$$

where a_i^l is the output of ReLU activation function $\sigma(x) = \max(0, x)$. W_{ij}^l and b_i^l are the weights and bias of neuron i in the l -th layer respectively.

b) Spiking Neuron Model: Integrate-and-Fire (IF) neuron model is widely used in conversion algorithms [29], [30], [42], [43], [45] because of the low computing cost and robust representation on firing rate. At each simulating time step t , the IF neuron i receives afferent spikes $s_i^{l-1}[t]$ and updates its state $u_i^l[t]$ by integrating the input potential $v_i^l[t]$:

$$u_i^l[t] = \hat{u}_i^l[t-1] + v_i^l[t] = \hat{u}_i^l[t-1] + \sum_j W_{ij}^l s_j^{l-1}[t] + b_i^l \quad (2)$$

where $u_i^l[t]$ and $\hat{u}_i^l[t]$ denote the membrane potential before and after reset respectively. The neuron generates a spike $s_i^l[t]$ and resets the membrane potential whenever $u_i^l[t]$ exceeds the firing threshold θ_i^l :

$$s_i^l[t] = \Theta(u_i^l[t] - \theta_i^l) \quad \text{with } \Theta(x) = \begin{cases} 1, & \text{if } x \geq 0 \\ 0, & \text{otherwise} \end{cases} \quad (3)$$

Specifically, we adopt the widely used soft-reset (reset-by-subtraction) mechanism [6], [42] rather than resetting as a

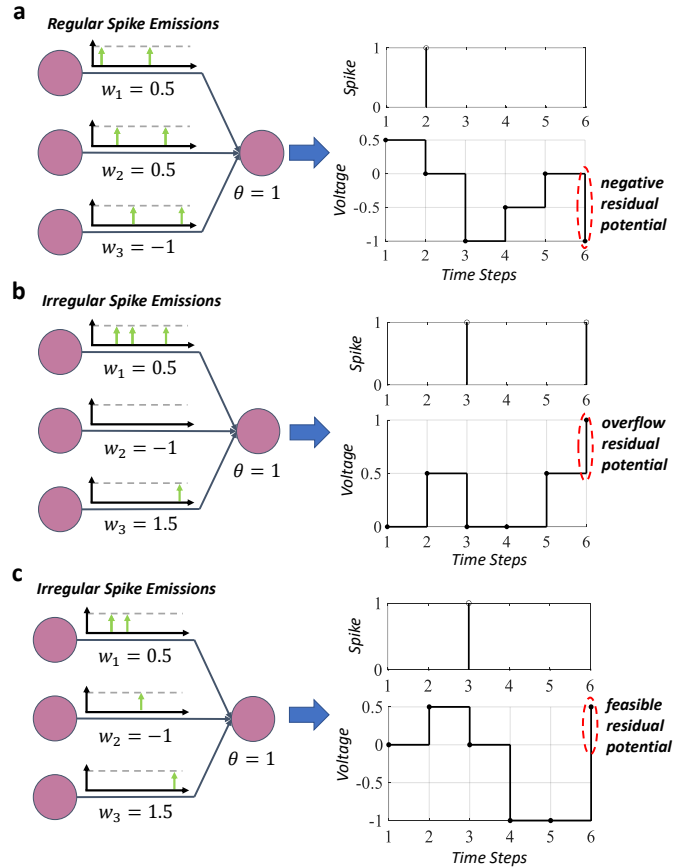


Fig. 2. Handcrafted examples under the cases of (a) regular spike emissions with an undervalued rate, (b) irregular spike emissions with an overvalued rate, and (c) irregular spike emissions with the correct rate, to explain the residual membrane potential representation error.

constant to reduce information loss from the membrane potential over the threshold. Formally, the soft reset mechanism is presented as:

$$\hat{u}_i^l[t] = u_i^l[t] - s_i^l[t] \cdot \theta_i^l \quad (4)$$

c) Fusing Batch Normalization: Batch normalization is a crucial component for most CNN architecture as it helps mitigate the internal covariate shift. The absence of batch normalization can be detrimental to network convergence and generalization. However, there is no direct equivalent module for batch normalization in SNNs as standard normalization methods damage the binary nature of spikes. Therefore, as done in most literature [26], [30], [31], [36], [41], [45], [46], we absorb the batch normalization on activations and transform it into batch normalization on weights and bias at the beginning, without detrimental effect on performance [52], [53]:

$$\begin{aligned} \text{BN}_w(W_{ij}^l) &= \frac{\gamma_i^l}{\sqrt{(\sigma_i^l)^2 + \epsilon}} W_{ij}^l \\ \text{BN}_b(b_i^l) &= \frac{\gamma_i^l}{\sqrt{(\sigma_i^l)^2 + \epsilon}} (b_i^l - \mu_i^l) + \beta_i^l \end{aligned} \quad (5)$$

where μ_i^l and σ_i^l represent the moving mean and moving variance of a_i^l estimated from batch statistics during training.

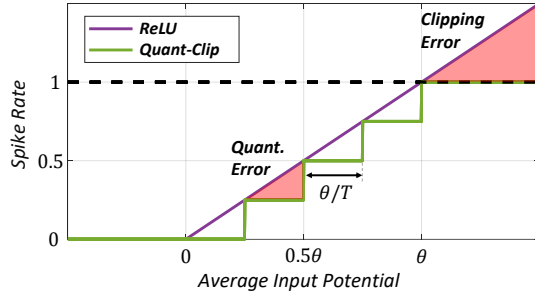


Fig. 3. A schematic diagram illustrating quantization and clipping errors controlled by threshold θ and time step T with spike rate representation.

γ_i^l and β_i^l are trainable parameters in the batch normalization layer.

d) Input and Readout: Instead of employing explicit spike coding, we opt to directly inject the image as input current repeatedly into SNNs at each time step, thereby avoiding information loss as done in [30], [54]. In essence, the first layer in SNNs is responsible for encoding the analog pixels into discrete spikes. Additionally, the average input potential $\bar{v}_i^l = (\sum_{t=1}^T v_i^l[t])/T$ rather than spike rate $r_i^l = (\sum_t s_i^l[t])/T$ is read out in the last layer.

IV. ERROR ANALYSIS

The goal of this paper is to build a consistent mapping between spike rates r_i^l in SNNs and activation values a_i^l in ANNs shown in Fig. 1. Firstly, we derive the exact relation between average input potential \bar{v}_i^l and input spike rate r_j^{l-1} :

$$\bar{v}_i^l = \frac{\sum_{t=1}^T \sum_j W_{ij}^l s_j^{l-1}[t] + b_i^l T}{T} = \sum_j W_{ij}^l r_j^{l-1} + b_i^l \quad (6)$$

Compared to Eq. 1, the functional relation between \bar{v}_i^l and r_j^{l-1} in IF neurons is identical to that between z_i^l and a_j^{l-1} in analog neurons. Then, the remaining question is what is the difference between the function $\bar{v}_i^l \rightarrow r_i^l$ and the function $z_i^l \rightarrow a_i^l$? By substituting Eq. 4 to Eq. 2 and accumulating from 0 to T , the relation between r_i^l and r_j^{l-1} is deduced as:

$$r_i^l = \sum_j (W_{ij}^l r_j^{l-1} + b_i^l) / \theta_i^l - \epsilon_i^l \quad (7)$$

where $\epsilon_i^l = \frac{\hat{u}_i^l[T] - \hat{u}_i^l[0]}{T\theta_i^l}$ is the component about residual membrane potential $\hat{u}_i^l[T]$. By substituting Eq. 6 into Eq. 7, we obtain the exact expression between \bar{v}_i^l and r_i^l :

$$r_i^l = f_{\theta,T}(\bar{v}_i^l, \epsilon_i^l) = \bar{v}_i^l / \theta_i^l - \epsilon_i^l \quad (8)$$

Remarkably, ϵ_i^l is highly nonlinear, nondifferentiable, and nonconvex as $\hat{u}_i^l[T]$ is calculated with the compound of T Heaviside functions $\Theta(x)$ explicated in Eqs. 2 - 4. Therefore, the only divergence of operators appears between the equivalent activation function $f_{\theta,T}(x, \epsilon)$ in SNNs and $\sigma(x)$ in ANNs. To bypass the non-determinism and complexity of ϵ , we start from the limited residual membrane potential assumption:

$$0 \leq \hat{u}_i^l[T] - \hat{u}_i^l[0] < \theta_i^l \quad (9)$$

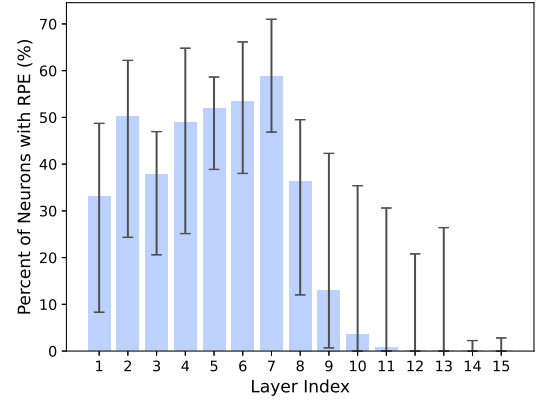


Fig. 4. The proportion of neurons with RPE in each layer of converted spiking VGG-16 on the CIFAR-10 dataset. The maximum deviations for all trials are reported, indicating the errors from negative or overflow potential.

Under such assumption, ϵ_i^l is bounded in $[0, \frac{1}{T})$ whereas $r_i^l \in \{\frac{0}{T}, \frac{1}{T}, \dots, \frac{T}{T}\}$. The nonlinearity of $f_{\theta,T}(x, \epsilon)$ can be approximated using the floor function with a quantization step of θ/T (indicated by the green line in Fig. 3):

$$g_{\theta,T}(x) = \frac{1}{T} \left\lfloor x \frac{T}{\theta} \right\rfloor = \frac{1}{\theta} \lfloor x \rfloor_{\theta/T} \quad (10)$$

Furthermore, the spike rate clipping technique is adopted to compensate for the error between $f_{\theta,T}(x)$ and $g_{\theta,T}(x)$ when the condition of Eq. 9 is not satisfied.

$$g_{\theta,T}(x) = \text{clip} \left(\frac{1}{\theta} \lfloor x \rfloor_{\theta/T}, 0, 1 \right) \quad (11)$$

However, the errors still exist and remain non-negligible even with such compensation. It is often attributed to transient dynamics [30], temporal jitter of spike trains [28], or unevenness error [37] without dedicated optimization. However, we contend that it is more precise and tractable to attribute such error to an incomplete representation of residual membrane potential rather than the irregular discharge of spikes in IF models. To illustrate this, we handcraft three examples under uniform and irregular spike distribution respectively in Fig. 2 as follows:

Example 1 (Regular Spike Emissions with Undervalued Rate). All the input neurons emit spikes regularly with an interval of 2 time steps in Fig. 2a. However, the output of floor-clipping function $g_{\theta,T}(\bar{v})$ is 0 while the real spike rate $r = f_{\theta,T}(\bar{v}, \epsilon)$ is $\frac{1}{6}$. The spike rate is undervalued with negative residual potential even under such uniform spike afferents.

Example 2 (Irregular Spike Emissions with Overvalued Rate). The output neuron is in a saturation state with a real spike rate $r = \frac{2}{6}$ while the expectation $g_{\theta,T}(v)$ is $\frac{3}{6}$ in the example of Fig. 2b. The spike rate is overvalued with overflow residual potential.

Example 3 (Irregular Spike Emissions with Correct Rate). The output neuron is in a state that yields the correct output rate $r = g_{\theta,T}(v) = \frac{1}{6}$ as shown in the example of Fig. 2c. The spike rate is estimated appropriately with feasible residual potential although the afferent spikes are irregular.

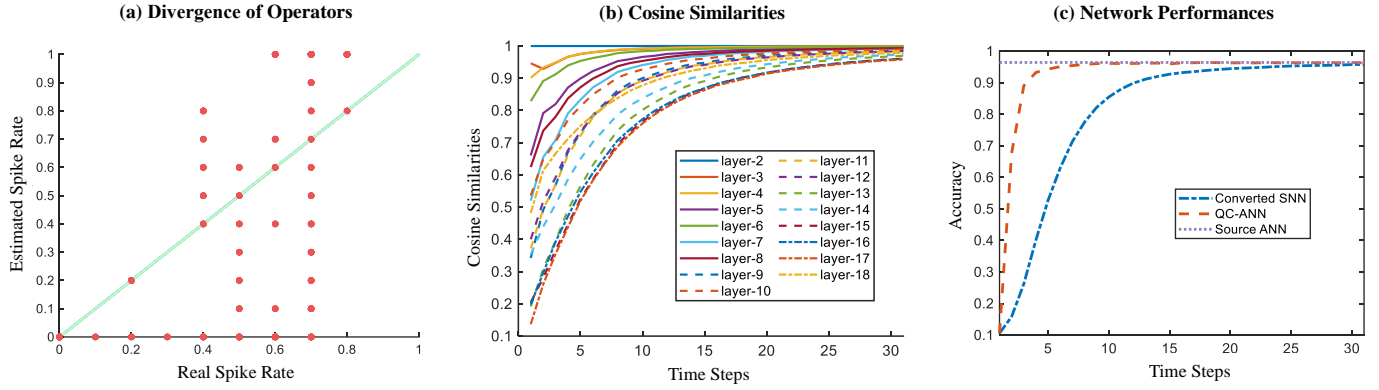


Fig. 5. Exploring the influence of RPE over QE and CE. (a) The non-identical relation between the estimated spike rate and the real spike rate. (b) The layer-wise cosine similarities between the activation of QC-ANN and the spike rate of converted SNN. (c) The accuracy gap between source ANN, QC-ANN, and converted SNN.

Therefore, the estimated spike rate may either surpass or fall below the actual rate of IF neurons in both cases as shown in Fig. 2a and Fig. 2b. In addition, the spike rate can also be evaluated exactly with irregular spike afferents (Fig. 2c). The fundamental cause of the error is that the IF neuron with soft-reset mechanism cannot respond to the residual membrane potential out of $[0, \theta]$. Then we refer to the kind of error as residual membrane potential representation error, RPE in short. It measures the divergence between the real spike rate $f_{\theta,T}(x, \epsilon)$ and the estimated spike rate $g_{\theta,T}(x)$ as shown in the left part of Fig. 1. Besides, the quantization and flooring function $g_{\theta,T}(x)$ is divergent from the ReLU function $\sigma(x)$ commonly used by ANNs in operators. Li *et al.* [26] summarized similar errors in the PSP-based conversion algorithm as clipping error and flooring error. Here we denote them as clipping error, CE and quantization error, QE generally shown in Fig. 3. Intuitively, RPE reflects the discrepancy that arises from the inherent differences in operating mechanisms between asynchronous SNNs (with temporal unfolding and over-threshold firing) and synchronous ANNs while QE represents the approximating error between binary spikes and real-value activation. We conducted an analysis to measure the occurrence of RPE in each layer of the converted spiking VGG16 network using 4 time steps. Each sample in CIFAR-10 was treated as a separate trial. We recorded the mean and maximum deviation for all trials. The results, depicted in Fig. 4, indicate that RPE occurs frequently in early layers. It is worth noting that RPE at a single layer has a cumulative effect on subsequent layers. Therefore, RPE is not rare and has a substantial impact on the overall conversion.

In order to explore the influence of RPE over QE and CE further, we adopt the neural network using a quantization-clipping activation function (Eq. 10) as an intermediate network called QC-ANN to explicitly separate two kinds of errors. Specifically, we convert ResNet-18 into its spiking version on the CIFAR-10 dataset and analyze the conversion errors empirically from three perspectives:

a) Perspective I (Divergence of Operators):

We generate 100 periodically injected sequences $\mathcal{V} = \{\mathbf{v}_1[t], \mathbf{v}_2[t], \dots, \mathbf{v}_{100}[t]\}$ where each sequence $\mathbf{v}[t]$

is sampled with 10 time steps from sine functions of different frequencies. By injecting each sequence as current into the single spiking neuron, we obtain the real spike rate \mathbf{r} through iterative equations (Eq. 2 - Eq. 3). Meanwhile, we adopt the quantization-clipping function $g_{\theta,T}(\frac{1}{T} \sum_t \mathbf{v}[t])$ to estimate the response spike rate $\hat{\mathbf{a}}$. As shown in Fig. 5a, there is a prominent bias compared to the identical mapping between $\hat{\mathbf{a}}$ and \mathbf{r} even in the ideal condition which illustrates the fundamental divergence of operators between $g_{\theta,T}(\bar{\mathbf{v}})$ and $f_{\theta,T}(\bar{\mathbf{v}}^l, \epsilon^l)$, i.e. RPE on the single neuron.

b) Perspective II (Error Accumulation): We calculate the cosine similarities ($\text{sim}(\mathbf{x}_1, \mathbf{x}_2) = \frac{\mathbf{x}_1 \mathbf{x}_2}{\|\mathbf{x}_1\|_2 \|\mathbf{x}_2\|_2}$) of activations between the source ANN and QC-ANN on 1024 samples to measure the error accumulation of RPE. This analysis serves to quantify the accumulation of RPE. Upon comparing the similarity curves of different layers (see Fig. 5b), we observe that shallower layers tend to exhibit higher similarities in general. It demonstrates that divergence of operations (RPE) in former layers brings cumulative errors through subsequent layers. Additionally, it is observed that the similarities gradually increase with the growth of the time step T . This phenomenon happens because, in this case, the residual term $\epsilon^l = \frac{\hat{\mathbf{u}}^l[T] - \hat{\mathbf{u}}^l[0]}{T\theta^l}$ diminishes progressively.

c) Perspective III (Performance Gap): To observe the performance gap resulting from cumulative errors, Fig. 5c displays the accuracy curves of source ANN, QC-ANN, and SNN over various time steps. The performance gap between QC-ANN and converted SNN demonstrates the conversion loss caused by neglected RPE about ϵ while the difference between QC-ANN and source ANN indicates the impact of QE and CE. It is worth noting that the error resulting from RPE generally makes greater contributions to the overall conversion error from source ANN to SNN than QE and CE.

The theory and experiments in the analysis above consistently show that RPE works in a complementary manner with respect to QE and CE. Additionally, as illustrated in Fig. 5c, the neglected RPE gives a wider optimization space for few time steps. Therefore, this phenomenon motivates us to rethink the conversion errors and redesign the algorithm exploiting the RPE.

V. METHOD

Based on the above error analysis, we propose a two-stage conversion scheme (Fig. 6) towards lossless conversion by minimizing QE, CE, and RPE in stages. Overall, we start from a source neural network using the clipping function $\sigma(x)$ as the activation function, then transfer it to a neural network with trainable quantization-clipping activation function $g_{\theta,T}(x)$, called QC-ANN later. Therefore, the QE and CE are optimized with the fine-tuning of the QC-ANN. Finally, the layer-wise calibration on weights and initial membrane potential is adopted to optimize the RPE based on the activation divergence between $g_{\theta,T}(x)$ and $f_{\theta,T}(\bar{v}_i^l, \epsilon_i^l)$.

A. Stage-I: QC-Finetuning with Trainable Threshold

The principle of the first stage is to minimize the QE and CE (right part of Fig. 1) and to take the quantization and clipping property of estimated activation function $g_{\theta,T}(x)$ for SNNs into ANN training. So we introduce the QC-ANN with trainable thresholds θ_i^l as the intermediate network.

Convert ANNs into QC-ANNs: To avoid the high computational cost due to training from scratch with QC activation function $g_{\theta,T}(x)$ under different T , we start with training source ANNs with activation $\sigma_{\theta}(x) = \text{clip}(\frac{1}{\theta}x, 0, 1)$ unrelated to the specified time steps T . Then we convert the source ANN into QC-ANN by simply copying the network parameters and replacing the corresponding activation functions. Here, we adopt a similar shift term $\Delta x = \theta/(2T)$ proposed in [31] to minimize the distance $\|\sigma_{\theta}(x) - g_{\theta,T}(x + \Delta x)\|^2$ under different time steps T . So the floor term in $g_{\theta,T}(x)$ in QC-ANN is replaced by a round term:

$$\begin{aligned} g_{\theta,T}(x) &= \text{clip}\left(\frac{1}{\theta}Q_{\theta/T}(x), 0, 1\right) \quad \text{where} \\ Q_{\Delta}(x) &= \Delta Q_1\left(\frac{x}{\Delta}\right) = \Delta \text{round}\left(\frac{x}{\Delta}\right) \end{aligned} \quad (12)$$

Fine-tuning with Quantization Noise: Although the optimal shift is applied, the QE and CE still exist and contribute to the conversion error. So we finetune the QC-ANN after copying weights from source ANN and replacing the activation function $\sigma_{\theta}(x)$ with $g_{\theta,T}(x)$. Notably, the round term $Q(x)$ in $g_{\theta,T}(x)$ has null gradients, which means the derivative of the input is zero almost everywhere. To train QC-ANN with such an ill-defined function, we adopt the widely used Straight Through Estimator (STE) [55] to estimate the gradients:

$$\frac{\partial Q_{\Delta}(x)}{\partial x} = \frac{\partial Q_1(x)}{\partial x} = \frac{\partial \lfloor x \rfloor}{\partial x} = 1 \quad (13)$$

Nevertheless, in the STE scheme, most weights are updated with biased gradients. It brings the larger bias with the increasing quantization step θ/T when the time step is relatively low ($T < 8$). Furthermore, the convergence of the QC-ANN and the fast-inference ability of converted SNNs are inevitably limited. Here we propose to correct the biased gradients using the noisy quantization function $\hat{Q}_{\Delta}(x)$ inspired by [56] which introduces Quant-Noise in model compression. Specifically,

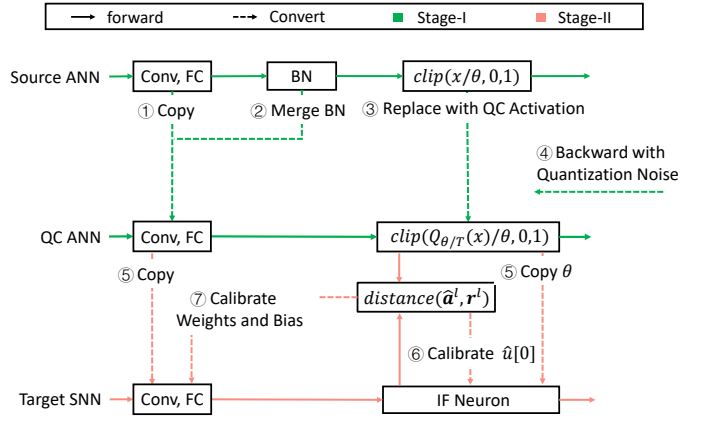


Fig. 6. The overall conversion framework incorporates a two-stage design to minimize threefold errors. The numbers within the circles represent the order of execution.

we replace a random fraction of $Q_{\Delta}(x)$ with the identity mapping x at each forward:

$$\begin{aligned} \hat{Q}_{\Delta}(x) &= x + (Q_{\Delta}(x) - x) \cdot M \\ \frac{\partial \hat{Q}_{\Delta}(x)}{\partial x} &= \frac{\partial Q_{\Delta}(x)}{\partial x} = 1 \end{aligned} \quad (14)$$

where $M \sim \text{Bernoulli}(p)$ is the random mask. Then we further modify Eq. 12 during QC-finetuning as:

$$g_{\theta,T}(x) = \text{clip}\left(\frac{1}{\theta}\hat{Q}_{\theta/T}(x), 0, 1\right) \quad (15)$$

Thus, most weights in QC-ANN are updated with unbiased gradients boosting the convergence under large quantization step.

B. Stage-II: Layer-wise Calibration with BPTT

After copying the weights, biases, and thresholds trained in QC-ANN into the target SNN, we get an SNN without considering RPE. To optimize RPE, the core objective of the second stage shown in the left part of Fig. 1, we adopt a layer-wise calibration mechanism on weights \mathbf{W} and initial membrane potential $\hat{u}[0]$. Firstly, we modify the real activation function $g_{\theta,T}(x)$ on spike rate accordingly with respect to the shift $\theta/(2T)$ adopted in $g_{\theta,T}(x)$:

$$f_{\theta,T}(\bar{v}, \epsilon) = \left(\bar{v} + \frac{\theta}{2T}\right) / \theta - \epsilon \quad (16)$$

By calibrating $f_{\theta,T}(\bar{v}, \epsilon)$ towards $g_{\theta,T}(\bar{v})$ further, we effectively narrow the performance gap without the need for specialized neuron design.

Coarse Calibration (CC) on Initial Membrane Potential: When the condition Eq. 9 is not satisfied, the initial membrane potential $\hat{u}^l[0]$ at the l -th layer plays a coarse adjustment role for the activation distribution as shown in Eq. 7. Considering the offline strategy of calibration-before-inference on N samples, the core for calibrating $\hat{u}[0]$ lies in solving the following optimization equation:

$$\min_{\hat{u}[0]} \left\{ \sum_{i=1}^N \left(\frac{\bar{v}_i}{\theta} + \frac{1}{2T} - \frac{\hat{u}_i[T] - \hat{u}[0]}{T\theta} - g_{\theta,T}(z_i) \right)^2 \right\} \quad (17)$$

Algorithm 1: Algorithm for the two-stage ANN-SNN conversion

Input : Source ANN model $\mathcal{F}_{ANN}(\mathbf{W}; \mathbf{x})$ with activation function $\sigma(x) = \text{clip}(\frac{1}{\theta}x, 0, 1)$;
 Dataset D ; Time step T ; Total epoch E

Output: SNN model $\mathcal{F}_{SNN}(\hat{\mathbf{W}}; \mathbf{x})$

```

1 /* Stage-I: QC-Finetuning */
2 Merge BN layers into weights and bias.
3 for each layer  $\mathcal{F}_{ANN}^l(\mathbf{W}; \mathbf{x})$  in  $\mathcal{F}_{ANN}(\mathbf{W}; \mathbf{x})$  do
4     if  $\mathcal{F}_{ANN}^l(\mathbf{W}; \mathbf{x})$  is instance of activation function
5          $\sigma_\theta(x)$  then
6             replace  $\sigma_\theta(x)$  with  $g_{\theta,T}(x)$  (Eq. 15) with the
7             shared parameter  $\theta$ 
8 Finetune the obtained  $\mathcal{F}_{QC-ANN}(\mathbf{W}; \mathbf{x})$  with  $g_{\theta,T}(x)$  as
9 activation function on  $D$ 
10 Copy weights from  $\mathcal{F}_{QC-ANN}(\mathbf{W}; \mathbf{x})$  into the SNN
11  $\mathcal{F}_{SNN}(\mathbf{W}; \mathbf{x})$  and introduce the shift  $\theta/2T$  (Eq. 16)
12 /* # Stage-II: Layer-wise Calibration with BPTT */
13 Sample a calibration subset  $\hat{D}$  from  $D$ 
14 for  $l \leftarrow 1$  to  $\mathcal{F}_{ANN}(\mathbf{W}; \mathbf{x}).layers$  do
15     for  $e \leftarrow 1$  to  $E$  do
16         for  $b \leftarrow 1$  to  $\hat{D}.batches$  do
17             Fetch the activation  $\hat{a}_b^l$  of  $\mathcal{F}_{QC-ANN}^l(\mathbf{W}; \mathbf{x})$ 
18             on calibration samples  $\hat{D}_b$ 
19             Fetch the input  $\mathbf{S}^l = [s_b^l[0], s_b^l[1], \dots, s_b^l[T]]$ 
20             of  $\mathcal{F}_{SNN}^l(\mathbf{W}; \mathbf{x})$  on calibration samples  $\hat{D}_b$ 
21             Feedforward on the spiking layer  $\mathcal{F}_{SNN}^l$ 
22             with  $\mathbf{S}^l$  and calculate the spike rate  $\mathbf{r}^l$ 
23             Calculate the gradients  $\frac{\partial \mathcal{L}}{\partial \mathbf{W}}$  and  $\frac{\partial \mathcal{L}}{\partial \mathbf{U}[0]}$  (Eq.
24             21)
25             Update  $\mathbf{W}$  and  $\mathbf{U}[0]$ 
26 return  $\mathcal{F}_{SNN}(\hat{\mathbf{W}}; \mathbf{x})$ 

```

Suppose $\hat{\mathbf{u}}[T]$ is unrelated to $\hat{\mathbf{u}}[0]$, then the problem turns into a linear form and the corresponding solution is:

$$\begin{aligned} \hat{\mathbf{u}}[0] &= \frac{T\theta}{N} \sum_{i=1}^N (g_{\theta,T}(z_i) - f_{\theta,T}(\bar{v}_i, \epsilon_i | \hat{\mathbf{u}}[0] = \mathbf{0})) \\ &= \frac{T\theta}{N} \sum_{i=1}^N (\hat{a}_i - \mathbf{r}_i) \end{aligned} \quad (18)$$

By the way, we can roughly correct the output expectation of the target SNN to match that of the QC-ANN. Additionally, CC has a relatively low calculation overhead that is proportionate to inference on N calibration samples.

Fine Calibration (FC) considering Temporal Dynamics:
 To calibrate the RPE more precisely, we measured the KL

TABLE I
 COMPARISON OF DATA AUGMENTATION, ENCODING, AND READOUT METHODS USED IN THE PROPOSED APPROACH AND OTHER BEST-PERFORMING METHODS. THE ABBREVIATIONS RC, RHF, C, AA, CJ, L, AND LS STAND FOR RANDOMCROP, RANDOMHORIZONTALFLIP, CUTOFF, AUTOAUG, COLORJITTER, LIGHTING, AND LABEL SMOOTHING, RESPECTIVELY.

Method	Data Augmentation		Encoding	Readout
	CIFAR	ImageNet		
QCFS[37]	RC, RHF, C, AA	RC, RF, CJ	Direct	Analog
RMP [6]	RC, RHF	RC, RHF, CJ, L	Rate	-
OPT [31]	RC, RHF, C, AA	RC,RHF,CJ	Direct	Analog
CAP [26]	RC, RHF, C, AA	RC,RHF,CJ	Direct	Analog
OPI [48]	RC,RHF, C, AA	RC,RHF, CJ, LS	Direct	Analog
RNL [46]	RC, RHF	-	Direct	-
Ours	RC, RHF, C, AA	RC, RHF	Direct	Analog

divergence between target activation \hat{a}^l and real spike rate \mathbf{r}^l in the recognition task:

$$\min_{\mathbf{W}} \mathcal{L}(\mathbf{r}^l, \hat{a}^l) = D_{KL}(\hat{a}^l \| \mathbf{f}_{\theta,T}(\bar{v}^l(\mathbf{W}), \epsilon^l(\mathbf{W}))) \quad (19)$$

Similarly, the MSE loss of Eq. 17 is adopted to improve the numerical precision of coordinate regression in object detection. Although \bar{v}^l is the linear combination of \mathbf{W}^l , ϵ^l is a superposition of nondifferentiable Heaviside functions $\Theta(x)$.

In order to solve such nonconvex and nondifferentiable optimization problems, we adopt a rectangular surrogate function $h(u)$ [54] to smooth the illness gradient $\frac{\partial \Theta(u)}{\partial u}$:

$$\frac{\partial \Theta(u)}{\partial u} \approx h(u) = \frac{1}{\alpha} \text{sign}\left(|u - \theta| < \frac{\alpha}{2}\right) \quad (20)$$

where α controls the smoothness degree for $\frac{\partial \Theta(u)}{\partial u}$. Then we obtain the gradients of weights with backpropagation-through-time (BPTT):

$$\begin{aligned} \frac{\partial \mathcal{L}}{\partial W_{ij}^l} &= \frac{1}{T} \frac{\partial \mathcal{L}}{\partial r^l} \sum_{t^*=1}^T \sum_{t=1}^{t^*} \frac{\partial s_i^l[t^*]}{\partial u_i^l[t]} s_j^{l-1}[t] \\ \frac{\partial \mathcal{L}}{\partial u_i^l[0]} &= \frac{1}{T} \frac{\partial \mathcal{L}}{\partial r^l} \sum_{t^*=1}^T \frac{\partial s_i^l[t^*]}{\partial u_i^l[0]} \\ \frac{\partial s_i^l[t^*]}{\partial u_i^l[t]} &= \begin{cases} h(u_i^l[t^*]) & \text{if } t = t^* \\ \frac{\partial s_i^l[t^*]}{\partial u_i^l[t+1]} (1 - \theta_i^l h(u_i^l[t])) & \text{if } t < t^* \end{cases} \end{aligned} \quad (21)$$

Compared to the direct training with surrogate gradients using BPTT, our calibration methods here only feedforward and backward on one layer which means the spatial complexity is $O(T \cdot \max_l(n_l))$ rather than $O(T \cdot \sum_l n_l)$ where n_l is the neurons number at the l -th layer in ANNs. Moreover, it is much easier and more computationally efficient to converge by fine-tuning on a pretrained layer rather than retraining from scratch on a large network presented in surrogate gradient methods. Empirically, it is enough for the calibration with several hundred of samples. The algorithm is illustrated in the pseudocode of Algorithm 1.

VI. EXPERIMENTS

In this section, we first evaluate the effectiveness and efficiency of the proposed method compared to other state-of-the-art conversion algorithms for image recognition tasks

TABLE II

THE TRADEOFF BETWEEN ACCURACY AND INFERENCE DELAY ON THE CIFAR-10 AND CIFAR-100 DATASETS. THE FORMAT "A/B" DENOTES THE REPRODUCED RESULT "A" AND THE REPORTED RESULT "B" IN THE ORIGINAL PAPER, WHEREAS ONLY "A" DENOTES THE REPORTED RESULT.

Dataset	Method	Architecture	ANN Acc.	$T = 2$	$T = 4$	$T = 8$	$T = 16$	$T = 32$	$T = 64$	$T \geq 128$
CIFAR-10	TSC [50] [†]	ResNet-20	91.47	-	-	-	-	-	69.38	91.42
	RMP [6] [†]	ResNet-20	96.60/91.47	10.00/-	10.00/-	10.30/-	62.38/-	91.99/-	95.62/-	96.22/91.36
	OPT [31]	ResNet-20	96.53/95.46	10.00/-	10.02/-	31.19/-	81.72/-	94.21/84.06	95.97/92.48	96.38/95.30
	CAP [26]	ResNet-20	96.89/95.46	67.24/-	80.86/-	90.44/-	94.08/-	95.95/94.78	96.44/95.30	96.66/95.45
	RNL [46]	PreActResNet-18	93.06/93.06	10.00/-	12.19/-	20.54/-	43.63/47.63	82.94/83.95	91.85/91.96	93.30/93.41
	OPI [48]	ResNet-18	96.51/96.04	34.47/-	49.94/-	73.79/75.44	91.02/90.43	95.59/94.82	96.37/95.92	96.61/96.08
	QCFS [37]	ResNet-18	96.04	75.44	90.43	94.82	95.92	96.08	96.06	96.06
	Ours	ResNet-18	96.41	89.97	93.27	95.36	96.28	96.44	96.49	96.43
		ResNet-20	96.66	90.43	93.27	95.46	96.30	96.60	96.71	96.76
	TSC [50]		93.63	-	-	-	-	-	92.79	93.63
	RMP [6]		95.81/93.63	10.00/-	10.00/-	10.00/-	26.89/-	81.13/60.30	93.34/90.35	95.45/93.63
	OPT [31]		95.59/95.72	10.00/-	10.00/-	45.35/-	91.55/-	94.66/76.24	95.43/90.64	95.53/95.73
	CAP [26]	VGG-16	95.75/95.72	77.78/-	85.37/-	90.82/-	93.41/-	94.72/93.71	95.35/95.14	95.62/95.79
	RNL [46]		92.81/92.82	10.00/-	10.00/-	11.17/-	52.91/57.90	85.00/85.40	91.04/91.15	92.52/92.51
	OPI [48]		95.59/94.57	68.37/-	88.03/-	93.05/90.96	94.74/93.38	95.42/94.20	95.51/94.45	95.55/94.55
QCFS [37]		95.52	91.18	93.96	94.95	95.40	95.54	95.55	95.59	
Ours	VGG-16	95.73	91.71	94.06	95.26	95.55	95.71	95.78	95.81	
CIFAR-100	RMP [6]		71.22	1.00/-	1.00/-	1.00/-	8.47/-	39.04/-	65.09/-	74.47/63.76
	OPT [31]		77.09/77.89	1.00/-	1.00/-	2.32/-	53.37/-	71.80/7.64	76.13/21.84	77.02/55.04
	CAP [26]	VGG-16	77.54/77.89	30.82/-	44.16/-	61.27/-	68.27/-	72.41/73.55	76.34/76.64	77.33/77.40
	OPI [48]		77.09/76.31	38.42/-	51.67/-	64.63/60.49	72.72/70.72	76.15/74.82	76.91/75.97	77.13/76.31
	QCFS [37]		76.28	63.79	69.62	73.96	76.24	77.01	77.10	77.08
	Ours	VGG-16	77.22	64.89	70.08	75.06	76.61	77.41	77.35	77.24
	TSC [50] [†]		68.72	-	-	-	-	-	-	58.42
	RMP [6] [†]	ResNet-20	80.99/68.72	1.00/-	1.00/-	1.03/-	3.99/-	51.40/27.64	75.25/46.91	79.63/57.69
	OPT [31]	ResNet-20	79.20/77.16	1.00/-	1.02/-	1.65/-	34.57/-	71.31/51.27	78.07/70.12	79.07/75.81
	CAP [26]		80.38/77.16	32.98/-	51.44/-	67.85/-	75.27/-	78.80/76.32	80.04/77.29	80.51/77.73
OPI [48]	ResNet-18	79.43/79.36	33.07/-	47.16/-	65.50/57.70	75.37/72.85	78.60/77.86	79.29/78.98	79.60/79.60	
QCFS [37]	ResNet-18	78.80	70.79	75.67	78.48	79.48	79.62	79.54	79.61	
Ours	ResNet-18	79.22	73.20	75.98	78.84	79.83	80.36	80.61	80.41	

The symbol † indicates using standard ResNet-20 architecture while others construct ResNet-20 by adding two more layers to the ResNet-18.

on CIFAR-10, CIFAR-100, and ImageNet datasets. Each component of the design is validated with a comprehensive ablation study. Subsequently, both sample efficiency and energy efficiency are examined in different time steps. Furthermore, we investigate spike-based object detection with the proposed two-stage pipeline in shortened time steps.

A. Implementation Details

a) Training of Source ANN: To obtain a high-performance source ANN trained with $\sigma_\theta(x) = \text{clip}(\frac{1}{\theta}x, 0, 1)$. In general, there are three approaches: (1) Training an ANN with clipping function $\sigma_\theta(x)$ directly as done in [31]. (2) training an ANN with ReLU function and then constrain the activations into $[0, 1]$ with weight-threshold balancing technique [29], [30], [32]. (3) Training an ANN with the rescaled clipping function $\sigma_\theta(x) = \text{clip}(x, 0, \theta)$ [38] and then fusing the scale factor θ into weights after training. In experiments, we adopt the first method for CIFAR-10. For CIFAR-100 and ImageNet, we use the third method to achieve higher performance.

b) Experiments Settings: For CIFAR-10 and CIFAR-100 datasets, we crop images into 32×32 with the padding of 4 pixels and flip them horizontally at random. Besides, as done

in [26], [37], we adopt the data augmentation of Cutout [57] and AutoAugment [58] to increase the generalization ability of source ANNs. For ImageNet, we adopt the standard pre-processing pipeline and crop images into 224×224 .

For training source ANN, we initialize the learning rate as 0.1 and then update it through the SGD optimizer with a momentum of 0.9. Meanwhile, the weight decay is set to $5e-4$ to regularize the network. Besides, the learning rate is set as $1e-4$ further to finetune QC-ANN. For CIFAR-10, the probability of quantization noise p is set as 0.1 and 0.2 when $T \leq 4$. Otherwise, no noise is injected into QC-ANNs. The p is set as 0.1 across all time steps on ImageNet and CIFAR-100 datasets. For Stage II, we observed that the errors tend to vary across different layers. Therefore, to address this issue and facilitate layer-wise calibration with BPTT presented in Stage-II, we opted to use the Adam optimizer with an adaptive learning rate. The initial learning rate is configured as $5e-4$ and $1e-4$ for recognition and detection tasks, respectively. The weight decay is set as 0. Moreover, we also adopt layer-wise BPTT calibration on the initial potential for the ImageNet dataset. For energy analysis, we sample 1024 samples and calculate the mean value and standard deviation of synaptic operations. Early stopping is also used to alleviate overfitting with a tolerance of 20 epochs.

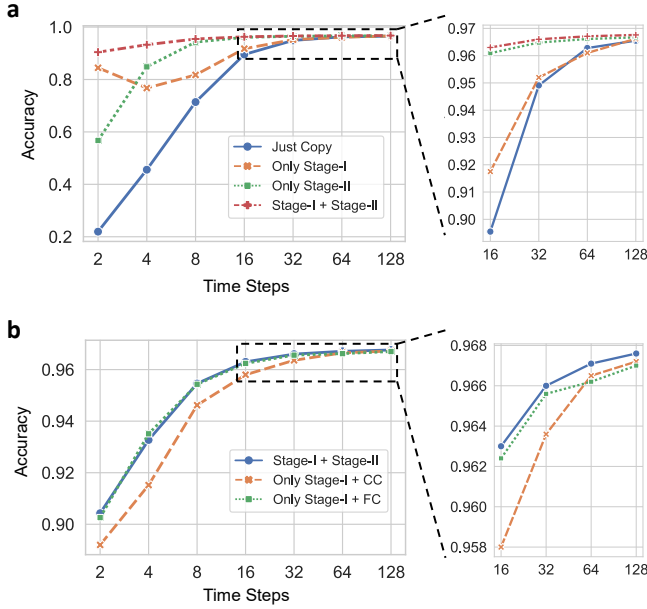


Fig. 7. Exploring the impact of individual components. (a) Each stage contributes to enhancing the performance in a complementary way. (b) The ablation study of the two calibration modules within Stage II.

c) *Evaluation Metrics*: For the task of object detection, we report the mean Average Precision (mAP) with different localization requirements. As an illustration, AP@0.75 denotes the mAP score which considers the predictions with a correct classification and localization IoU ≥ 0.75 as the true positive. Furthermore, according to the size of the ground truth, the mAP is divided into that of small objects AP_S, middle objects AP_M, and large objects AP_L.

B. Ablation Study

In this section, we conduct a series of ablation studies and show the proposed method reduces the conversion loss in a complementary manner. Specifically, we test ResNet-20 on CIFAR-10 from $T = 2$ to $T = 128$ under six conditions: *Just Copy Weights*, *Only Stage-I*, *Only Stage-II*, *Stage-I + Stage-II*, *Stage-I + CC*, and *Stage-I + FC*.

As shown in Fig. 7a, both *Only Stage-I* and *Only Stage-II* improve the performance effectively, which is especially impressive when $T \leq 32$. Besides, *Stage-I + Stage-II* with dedicated optimization obtains the best results across all time steps which indicates the synergic effect of the two stages. Comparing the two stages individually, we find *Stage-I* optimizing the QE and CE achieves better results when $T < 4$. Otherwise, *Stage-II* optimizing RPE mainly obtains higher performance. It is interpretable as the quantization factor θ/T and the QE naturally grow as T decreases. So the performance degradation stemmed from the QE plays a dominant role compared to RPE when T is extremely low. Surprisingly, *Only Stage-II* only needs 8 time steps to match the performance of *Stage-I + Stage-II*, whereas *Only Stage-I* requires 32 time steps. It demonstrates that optimizing RPE is more efficient in low-latency conversion in general. So simply adopting layer-wise Stage-II with a handful of samples is enough for

TABLE III
COMPARING RELATIVE PERFORMANCE LOSS UNDER $T = 32, 64,$ AND 128 ON IMAGENET DATASET.

Method	Architecture	$(\text{Acc}_{\text{ANN}} - \text{Acc}_{\text{SNN}}) / \text{Acc}_{\text{ANN}}$		
		$T = 32$	$T = 64$	$T = 128$
QCFS [37]	ResNet-34	6.66%	2.65%	1.57%
RMP [6]		98.35%	56.91%	15.09%
Norm-on-Shortcut [45]		89.74%	34.71%	8.04%
TCL [38]		98.64%	72.82%	14.20%
OPT [31]		93.61%	35.69%	7.08%
CAP [26]		10.40%	3.89%	1.65%
Ours	ResNet-34	2.41%	1.06%	0.08%
RMP [6]	VGG-16	99.57%	87.21%	31.72%
OPT [31]		98.53%	69.62%	13.58%
CAP [26]		11.45%	5.64%	2.82%
SNM [39]		11.48%	2.30%	0.44%
Burst [41] †		4.93%	1.28%	0.38%
QCFS [37]		7.83%	1.94%	0.43%
OPI [48]		13.56%	3.18%	0.81%
Ours		VGG-16	1.92%	0.27%

† denotes the method adopts multi-bit outputs rather than binary outputs.

conversion on resource-constrained devices. Notably, there is a strange accuracy drop for *Only Stage-I* when $T = 4$. It may come from increasing RPE which is not optimized by Stage-I. As shown in the curve of *Stage-I + Stage-II*, the drop is eliminated by introducing Stage-II (minimizing RPE). This indeed supports the efficacy of minimizing RPE.

To understand the effect of each component in Stage-II further, we do coarse calibration and fine calibration separately after Stage-I (Fig. 7b). In general, both components improve performance consistently. In particular, we find *Stage-I + FC* achieves extremely close results to *Stage-I + Stage-II*. And it even outperforms *Stage-I + Stage-II* when $T = 4$. Nevertheless, coarse calibration still provides a lightweight solution without gradient computation and a proper initialization for fine calibration.

C. Tradeoff between Accuracy and Inference Delay

We compare the proposed method with the state-of-the-art ANN-SNN conversion methods on CIFAR-10, CIFAR-100 (Table II), and ImageNet (Table IV) datasets. Here, in order to better compare the performance with different methods, we provide reproduced experimental results under few time steps in the format of "A/B".

In general, the proposed method achieves the best result nearly across all time steps. For ultra-low latency $T = 2$ and $T = 4$, our method achieves promising performance improvements of 14.53% and 2.84% with ResNet-18 on the CIFAR-10 dataset respectively. Notably, SNNs perform better than ANNs when time step increases up to 128 as shown in Table II. The identified residual potential error (RPE) in this work explains the underlying cause. The spike rate is used in conversion to approximate ANN activation. Typically, it is difficult to eliminate the non-deterministic component (i.e., the RPE) of approximation error. Thus, RPE serves as noise when using the firing rate of SNNs to replace the ANN activations (Eq. 8). The noise becomes the optimizing objective in Stage-II, and weights and initial potential are finetuned against such

TABLE IV

THE TRADEOFF BETWEEN ACCURACY AND INFERENCE DELAY ON IMAGENET DATASET. THE FORMAT "A/B" DENOTES THE REPRODUCED RESULT "A" AND THE REPORTED RESULT "B" IN THE ORIGINAL PAPER, WHEREAS ONLY "A" DENOTES THE REPORTED RESULT.

Method	Architecture	ANN Acc.	$T = 4$	$T = 8$	$T = 16$	$T = 32$	$T = 64$	$T = 128$	$T = 256$
TSC [50]		70.64	-	-	-	-	-	-	55.65
QCFS [37]		74.32	-	-	59.35	69.37	72.35	73.15	73.37
RMP [6]		74.54/70.64	0.10/-	0.10/-	0.10/-	1.23/-	32.12/-	63.29/-	71.20/55.65
Norm-on-Shortcut [45]	ResNet-34	74.54/72.88	0.13/-	0.20/-	0.70/-	7.65/-	48.67/-	68.55/-	72.75/-
TCL [38]		73.43/70.85	0.09/-	0.10/-	0.18/-	1.00/-	19.96/-	63.00/-	72.57/-
OPT [31]		73.43/75.66	0.10/-	0.10/-	0.15/-	4.69/0.09	47.22/0.12	68.23/3.19	72.37/47.11
CAP [26]		75.65/75.66	1.68/-	23.82/-	52.72/-	67.78/64.54	72.71/71.12	74.40/73.45	74.92/74.61
Ours	ResNet-34	73.43	55.71	61.20	67.77	71.66	72.65	73.37	73.45
TSC [50]		73.49	-	-	-	-	-	-	69.71
RMP [6]		74.53/73.49	0.08/-	0.09/-	0.13/-	0.32/-	9.53/-	50.89/-	68.78/48.32
OPT [31]		74.88/75.36	0.10/-	0.11/-	0.21/-	1.10/0.114	22.75/0.118	64.71/0.122	72.81/1.81
CAP [26]	VGG-16	74.53/75.36	5.65/-	25.70/-	56.25/-	66.0/63.64	70.33/70.69	72.43/73.32	73.54/74.23
SNM [39]		73.18	-	-	-	64.78	71.50	72.86	-
Burst [41]		74.27	-	-	-	70.61	73.32	73.99	74.25
QCFS [37]		74.29	-	-	50.97	68.47	72.85	73.97	74.22
OPI [48]		74.85	-	6.25	36.02	64.70	72.47	74.24	74.62
Ours	VGG-16	74.88	59.95	62.51	70.13	73.44	74.68	74.93	74.94

TABLE V

COMPARISON WITH DIRECT TRAINING WITH SPIKE-BASED BACKPROPAGATION.

Method	Architecture	Time Steps	Accuracy (%)
CIFAR-10			
BRP [59] †	2D-CSNN	-	57.08
STBP [54]	CIFARNet	12	90.53
Hybrid [60]	ResNet-20	250	92.22
DIET-SNN [61]	ResNet-20	5	91.78
TSSL [19]	CIFARNet	5	91.41
STBP-tDBN [62]	CIFARNet	4	92.92
Ours	ResNet-20	4	93.27
	VGG-16	4	94.06
CIFAR-100			
Hybrid [60]	VGG-11	125	67.87
DIET-SNN [61]	VGG-16	5	69.67
STBP-tDBN [62]	ResNet-19	4	70.86
Ours	ResNet-18	4	75.98
	VGG-16	4	70.08

The symbol † indicates that the method incorporates a biologically plausible pseudo-backpropagation approach, leveraging spike-timing-dependent plasticity (STDP).

noise, so that the RPE brings additional generalization ability to converted SNNs which their ANN counterparts do not have. The superiority seems to vanish when $T \geq 8$ compared to the most recent work [37]. However, when considering large-scale datasets like ImageNet, the proposed method still improves the state-of-the-art of accuracy-delay tradeoff sustainedly as explicated in Table. IV. For instance, the inference delay is shrunk by $4 \times$ into 4 time steps on ImageNet with VGG16 architecture while still obtaining significant performance improvements (8.98% top-1 at least, 59.95% vs. 50.97%) compared to the existing literature. Notably, as we do not apply the CollorJitter data augmentation as done in [26], [48], the result of source ANN on ImageNet and the best SNN ($T \geq 256$) is slightly lower than the best results reported [26]. Even though, our

TABLE VI

THE EFFECT OF THE NUMBER N OF CALIBRATION SAMPLES. THE NUMBER IN PARENTHESES IMPLIES THE ACCURACY OF THE SOURCE ANN.

# samples	ResNet-18 (96.41)			VGG-16 (95.73)		
	$T = 2$	$T = 4$	$T = 8$	$T = 2$	$T = 4$	$T = 8$
0	76.01	66.52	84.17	88.89	92.89	92.72
2	75.55	32.20	74.47	47.54	17.25	84.01
4	83.46	80.26	90.42	82.92	51.22	91.75
8	85.79	87.67	93.21	89.04	88.81	93.24
16	87.89	90.47	94.31	88.96	91.79	94.31
32	88.75	91.94	94.89	90.21	93.24	94.41
64	89.56	92.40	94.85	90.59	93.19	94.80
128	89.74	92.18	95.07	90.91	93.54	95.01
256	89.51	92.77	95.29	90.80	94.04	95.02
512	89.89	92.96	95.31	91.41	94.13	95.22
1024	90.49	93.23	95.35	90.98	93.60	95.04

method still outperforms previous works and achieves 74.68% top-1 accuracy under relatively long time steps ($T = 64$). A full comparison of data augmentation methods, encoding, and decoding methods with the best-performing competitors is provided in Table I.

It is worth noting that different methods use different source ANN activation functions (e.g., clipping function in TCL[38]) and different training methods (e.g., customized auxiliary loss for RNL layer in [46]). Hence, achieving exactly the same ANN performance, even with the same data preprocessor and optimizer, is challenging. To further eliminate the influence of the source ANN, we assess the relative performance losses $\Delta_{\text{Acc}} = (\text{Acc}_{\text{ANN}} - \text{Acc}_{\text{SNN}}) / \text{Acc}_{\text{ANN}}$ at $T = 32$, $T = 64$, and $T = 128$, as demonstrated in Table III. In general, the proposed method significantly reduces the conversion loss and enhances the performance of target SNNs. Moreover, as shown in Table V, our method is also competitive compared to the state-of-the-art direct training method characterized by temporal credit assignment under only 4 time steps on both CIFAR datasets. All those results illustrate the effectiveness

TABLE VII

COMPARING THE ENERGY COST UNDER DIFFERENT TIME STEPS ON CIFAR-100. THE NUMBERS IN PARENTHESES REPRESENT RELATIVE ACCURACY LOSSES DURING CONVERSION.

Metrics	Method	ANN	$T = 2$	$T = 4$	$T = 8$
Accuracy (%)	OPI [48]	79.43	33.07(73.49)	47.16(40.63)	65.50(17.54)
	CAP [26]	78.89	38.37(51.36)	53.96(31.60)	64.87(17.77)
	QCFS[37]	77.75	57.05(26.62)	67.28(13.47)	73.57(5.38)
	Ours	79.22	73.20(7.60)	75.98(4.09)	78.84(0.48)
GSOP ($\times 1e-3$)	OPI [48]	480.2	83.4 \pm 4.0	159.0 \pm 8.3	309.4 \pm 17.5
	CAP [26]	480.2	159.1 \pm 4.5	236.5 \pm 9.1	368.0 \pm 23.2
	QCFS[37]	480.2	138.7 \pm 6.2	266.5 \pm 14.1	522.1 \pm 30.3
	Ours	480.2	156.1 \pm 6.3	238.9 \pm 10.0	433.7 \pm 17.2
Energy (μ J)	OPI [48]	2208.7	75.1 \pm 3.6	143.1 \pm 7.4	278.5 \pm 15.7
	CAP [26]	2208.7	143.2 \pm 4.0	212.9 \pm 8.2	331.2 \pm 20.9
	QCFS[37]	2208.7	124.8 \pm 5.6	239.8 \pm 12.7	469.9 \pm 27.2
	Ours	2208.7	140.5 \pm 5.7	215.0 \pm 9.0	356.0 \pm 21.7
Energy Ratio(%)	OPI [48]	100	3.40 \pm 0.16	6.48 \pm 0.34	12.61 \pm 0.71
	CAP [26]	100	6.48 \pm 0.18	9.64 \pm 0.37	15.00 \pm 0.95
	QCFS[37]	100	5.65 \pm 0.25	10.86 \pm 0.57	21.27 \pm 1.23
	Ours	100	6.36 \pm 0.26	9.73 \pm 0.41	16.11 \pm 0.98

of optimizing threefold errors simultaneously.

D. Effect of Different Sample Numbers

As shown in Table VI, we investigate the impact of calibration sample numbers on CIFAR-10 using ResNet-34 and VGG-16 architectures. The initial line shows the baseline results without calibration. Interestingly, a small number of calibration samples yield significant enhancements. For instance, calibration on just 32 samples elevates the performance of spiking ResNet-18 by 25.42% when executed under 4 time steps, demonstrating the sample efficiency of the proposed calibration approach, particularly for low-latency conversion. It is worth mentioning that inadequate sample numbers may cause a certain decline in performance due to the randomness of BPTT calibration. In our experience, using 64 calibration samples leads to considerable performance improvement under low inference steps. During actual deployment, an appropriate calibration number can be obtained further by analyzing the regression curve of performance gains with respect to calibration samples.

E. Energy-Efficiency and Sparsity

HereIn this section, we count the total synaptic operations (SOP) to estimate the computation overhead of SNN compared to their ANN counterparts [9]. Especially, synaptic operation by accumulation (AC) in SNNs is variable with spike sparsity while synaptic operation by multiply and accumulation (MAC) in ANNs is constant given a particular network structure. Here, we measure 32-bit float-point AC and MAC by $\alpha_{AC} = 0.9 pJ$ and $\alpha_{MAC} = 4.6 pJ$ per operation individually as done in [63]. Notably, the estimation is extremely conservative and the energy consumption of SNNs on specified hardware design can be reduced by $12\times$ to $77 fJ/SOP$ [64].

From Table VII, SNN is more SOP-efficient with sparse spike communications than the ANN in the same ResNet-18

TABLE VIII

SCALING THE PROPOSED METHOD TO RESNEXT29-2X64D AND MOBILENETV2 ARCHITECTURES.

Method	ResNeXt29-2x64d (96.55)		MobileNetV2 (95.29)	
	$T = 8$	$T = 16$	$T = 16$	$T = 32$
Baseline	27.60	49.74	15.59	29.36
Stage-I	79.17	92.43	26.16	54.17
Stage-II	62.96	83.92	60.42	88.63
Stage-I + Stage-II	90.02	94.33	75.64	91.49

TABLE IX

SCALING THE PROPOSED METHOD TO LEAKY ReLU.

Method	VGG-16 (95.62)		ResNet-18 (96.81)	
	$T = 4$	$T = 8$	$T = 4$	$T = 8$
Baseline	47.77	71.80	71.46	87.49
Stage-I	78.83	82.47	88.27	91.55
Stage-II	86.02	91.48	85.44	92.52
Stage-I + Stage-II	91.76	93.38	91.23	93.93

architecture. The energy efficiency is more significant considering the operation degrading from MAC to AC. For instance, the conversion is nearly lossless (0.38% accuracy loss) when $T = 8$ with only 16% energy consumption compared to the ANN counterpart. For edge devices with stringent power requirements, the energy consumption is downgraded to 140 μ J further ($15.7\times$ energy saving with 73%+ performance on CIFAR-100). We further compare the energy consumption with the state-of-the-art methods [26], [37], [48]. In this analysis, we ensured that different methods were reproduced under the same conditions, and we used the same set of 1024 samples to estimate the power consumption. As shown in Table VII, although our approach consumes slightly more energy compared to OPI [48], it is justified by the significant performance gains achieved at few time steps. Specifically, our method reduces the relative performance loss (Δ_{Acc}) by 65.89% under 2 time steps.

F. Extensibility for Complex Structures

To demonstrate that our method can be applied to more complex models, we conduct ablation studies on the complex ResNeXt29-2x64d [65] and MobileNetV2 [66] structure. As shown in the VIII, for both advanced models, the proposed two-stage approach effectively improves the performance of the converted SNN at each stage and operates in a complementary manner. This further confirms the efficiency and adaptability of our technique in handling complex network architectures.

Moreover, the applicability of the proposed method extends beyond ReLU-based ANNs to encompass other activation functions, including Leaky ReLU. To achieve this, we follow similar derivations as presented in Section IV. Specifically, we utilize spiking neurons with asymmetric thresholds, as described in [40], and update the QC function, denoted by Eq. 11, as follows:

$$g_{\theta,T}(x) = \text{clip} \left(\frac{1}{\theta} [\text{LeakyReLU}(x)]_{\theta/T}, -1, 1 \right) \quad (22)$$

TABLE X
IMPROVING THE PERFORMANCE OF SPIKE-BASED OBJECT DETECTORS THROUGH THE PROPOSED METHOD.

Methods	Time Step	AP@0.50:0.95	AP@0.50	AP@0.75	AP _S	AP _M	AP _L
Spiking YOLO [32]		0.2	0.7	0.1	0.2	0.5	0.1
Stage-I w/out Stage-II	20	7.3	19.7	3.1	3.6	6.8	8.7
Stage-I + Stage-II		28.5	64.1	19.5	6.2	16.2	33.5
Spiking YOLO [32]		7.9	22.3	3.1	2.9	5.2	10.3
Stage-I w/out Stage-II	40	20.1	48.5	11.6	4.6	13.0	24.4
Stage-I + Stage-II		30.7	66.4	22.5	7.2	17.8	36.1
Spiking YOLO [32]	2000	26.9	59.9	19.1	6.7	15.5	31.6
Spiking YOLO [32]	60	16.5	41.6	8.2	5.3	9.2	20.1
Stage-I w/out Stage-II	60	25.7	58.7	16.6	5.7	15.6	30.6
Stage-I + Stage-II	60	31.2	66.8	23.2	7.1	17.9	36.7

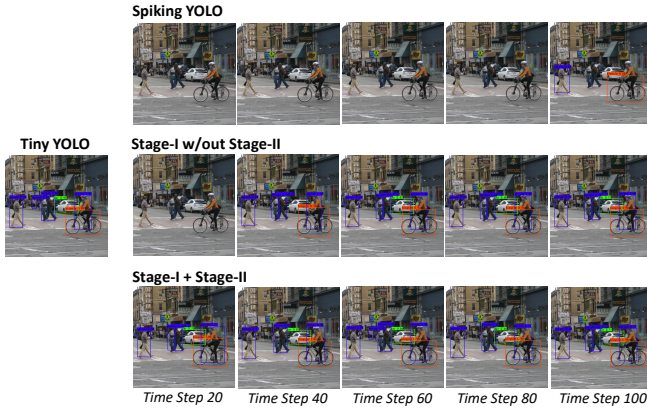


Fig. 8. The comparison of detection results on a single sample with increasing time steps.

The results of this adaptation are showcased in Table IX, where we observe a significant improvement in the performance of the converted SNN by stages. Additionally, the latency is dramatically reduced to 8 time steps, marking a substantial advancement compared to the typical state-of-the-art method [40] for conversion with the LeakyReLU activation function, which reports latencies in the hundreds of time steps.

G. Improvements on Object Detection

In this section, we investigate the effect of the proposed method on a more challenging detection task that involves the coordinate regression of bounding boxes and so requires higher numerical precision than object recognition to approximate the accurate coordinates. For a fair comparison, we implement the well-known spike-based object detector (Spiking YOLO [32]) in the same architecture which achieves better performance than that reported in the original paper. As depicted in Table X, the proposed method improves continuously the performance of spike-based detection across different object scales and time steps on the PASCAL VOC dataset. Meanwhile, the detection delay is reduced significantly by at least 25 times to 40 time steps for nearly lossless conversion while SpikingYOLO typically needs thousands of time steps. Moreover, Stage-I + Stage-II under few time steps (e.g. 20 time steps) outperforms Stage-I w/out Stage-II by a large margin, especially on the large and middle object detection (33.5% vs. 8.7%, 16.2%

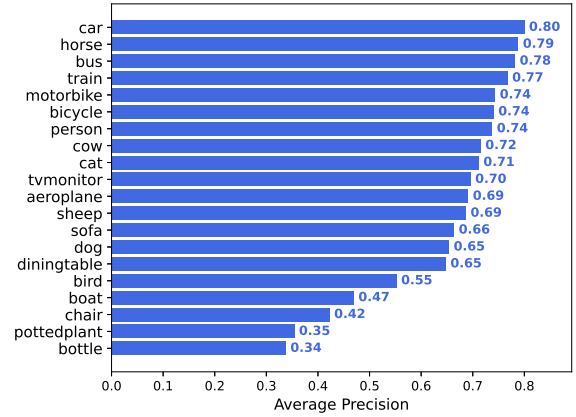


Fig. 9. Average detection precision for each class in 30 time steps.

vs. 6.8%). It further illustrates the effect of Stage-II and the importance of optimizing RPE in addition to QE and CE.

Furthermore, we show the detection results on a sample image with increasing time steps (Fig. 8). The far left gives the result of ANN-based Tiny YOLO. The top row displays the detection results of Spiking YOLO [32]. In this example, no object can be detected until the time step grows to 100. By optimizing QE and CE, Stage-I shortens the detection delay to 40 time steps although the numerical precision is still not high. The delay is further reduced to 20 time steps and higher detection accuracy is attained by further optimizing RPE in Stage-II. We also draw the detection results of each class of objects, as shown in Fig. 9.

VII. CONCLUSION AND DISCUSSION

In this work, instead of merely optimizing quantization and clipping error as in the previous works, this work first explicitly identifies the errors from residual potential which exhibit a more substantial role in low-latency conversion. By including an additional finetuning stage to specifically minimize this source of error, this study presents a novel two-stage converting strategy and obtains high-accuracy and low-latency SNNs. The introduced calibration mechanism considering temporal dynamics in SNNs effectively smooths the information loss of knowledge transfer between ANNs and SNNs. Experiments on large-scale recognition and detection tasks demonstrate our method improves both performance and latency greatly

with attractive power conservation compared to ANNs, which would facilitate the future application of SNNs on resource-constrained edge devices. Additionally, each module within the pipeline has undergone meticulous testing, including ablation studies, to ascertain its effectiveness and efficiency. For example, attractive performance improvements were achieved by calibrating with dozens of samples. We hope that by presenting a fresh perspective on conversion error, this study will help pave the road toward lossless ANN-SNN conversion under extremely low latency.

The proposed conversion method has limitations in processing time-domain data with RNN-like and attention-based architectures. In future work, we expect to adapt the concept of temporal calibration to other types of network structures, such as LSTM and Transformer. Additionally, we consider conversion methods based on temporal coding with BPTT calibration, aiming for ultimate energy efficiency and minimized latency. It is important to note that the proposed conversion method is not applicable to online or on-chip learning, as the conversion algorithms generally do not target online or on-chip learning with neuromorphic uses. Instead, they are widely applicable in efficient inference with lightweight parameter tuning. Therefore, how to realize transfer learning from ANNs to SNNs in a flexible, local, and online way is a worthwhile avenue for future research, especially in the context of deployment on neuromorphic chips.

REFERENCES

- [1] A. L. Hodgkin and A. F. Huxley, "A quantitative description of membrane current and its application to conduction and excitation in nerve," *The Journal of Physiology*, vol. 117, no. 4, p. 500, 1952.
- [2] W. Gerstner, R. Ritz, and J. L. Van Hemmen, "Why spikes? Hebbian learning and retrieval of time-resolved excitation patterns," *Biological Cybernetics*, vol. 69, no. 5, pp. 503–515, 1993.
- [3] W. Maass, "Networks of spiking neurons: the third generation of neural network models," *Neural Networks*, vol. 10, no. 9, pp. 1659–1671, 1997.
- [4] K. Roy, A. Jaiswal, and P. Panda, "Towards spike-based machine intelligence with neuromorphic computing," *Nature*, vol. 575, no. 7784, pp. 607–617, 2019.
- [5] D. V. Christensen, R. Dittmann, B. Linares-Barranco, A. Sebastian, M. Le Gallo, A. Redaelli, S. Slesazeck, T. Mikolajick, S. Spiga, S. Menzel *et al.*, "2022 roadmap on neuromorphic computing and engineering," *Neuromorphic Computing and Engineering*, vol. 2, no. 2, p. 022501, 2022.
- [6] B. Han, G. Srinivasan, and K. Roy, "RMP-SNN: Residual membrane potential neuron for enabling deeper high-accuracy and low-latency spiking neural network," in *Proceedings of the IEEE/CVF Conference on Computer Vision and Pattern Recognition*, 2020, pp. 13 558–13 567.
- [7] E. Painkras, L. A. Plana, J. Garside, S. Temple, F. Galluppi, C. Patterson, D. R. Lester, A. D. Brown, and S. B. Furber, "SpiNNaker: A 1-W 18-core system-on-chip for massively-parallel neural network simulation," *IEEE Journal of Solid-State Circuits*, vol. 48, no. 8, pp. 1943–1953, 2013.
- [8] M. Davies, A. Wild, G. Orchard, Y. Sandamirskaya, G. A. F. Guerra, P. Joshi, P. Plank, and S. R. Risbud, "Advancing neuromorphic computing with Loihi: A survey of results and outlook," *Proceedings of the IEEE*, vol. 109, no. 5, pp. 911–934, 2021.
- [9] P. A. Merolla, J. V. Arthur, R. Alvarez-Icaza, A. S. Cassidy, J. Sawada, F. Akopyan, B. L. Jackson, N. Imam, C. Guo, Y. Nakamura *et al.*, "A million spiking-neuron integrated circuit with a scalable communication network and interface," *Science*, vol. 345, no. 6197, pp. 668–673, 2014.
- [10] L. Deng, Y. Wu, X. Hu, L. Liang, Y. Ding, G. Li, G. Zhao, P. Li, and Y. Xie, "Rethinking the performance comparison between SNNs and ANNs," *Neural Networks*, vol. 121, pp. 294–307, 2020.
- [11] Y. Wu, L. Deng, G. Li, J. Zhu, and L. Shi, "Spatio-temporal backpropagation for training high-performance spiking neural networks," *Frontiers in Neuroscience*, vol. 12, p. 331, 2018.
- [12] S. B. Shrestha and G. Orchard, "SLAYER: Spike layer error reassignment in time," *Advances in Neural Information Processing Systems*, vol. 31, 2018.
- [13] E. O. Neftci, H. Mostafa, and F. Zenke, "Surrogate gradient learning in spiking neural networks: Bringing the power of gradient-based optimization to spiking neural networks," *IEEE Signal Processing Magazine*, vol. 36, no. 6, pp. 51–63, 2019.
- [14] P. Gu, R. Xiao, G. Pan, and H. Tang, "STCA: Spatio-temporal credit assignment with delayed feedback in deep spiking neural networks," in *IJCAI*, 2019, pp. 1366–1372.
- [15] W. Fang, Z. Yu, Y. Chen, T. Huang, T. Masquelier, and Y. Tian, "Deep residual learning in spiking neural networks," *Advances in Neural Information Processing Systems*, vol. 34, pp. 21 056–21 069, 2021.
- [16] S. M. Bohte, J. N. Kok, and J. A. La Poutré, "SpikeProp: Backpropagation for networks of spiking neurons," in *ESANN*, vol. 48. Bruges, 2000, pp. 419–424.
- [17] J. Kim, K. Kim, and J.-J. Kim, "Unifying activation-and timing-based learning rules for spiking neural networks," *Advances in Neural Information Processing Systems*, vol. 33, pp. 19 534–19 544, 2020.
- [18] Q. Yu, H. Li, and K. C. Tan, "Spike timing or rate? neurons learn to make decisions for both through threshold-driven plasticity," *IEEE Transactions on Cybernetics*, vol. 49, no. 6, pp. 2178–2189, 2018.
- [19] W. Zhang and P. Li, "Temporal spike sequence learning via backpropagation for deep spiking neural networks," *Advances in Neural Information Processing Systems*, vol. 33, pp. 12 022–12 033, 2020.
- [20] A. Taherkhani, A. Belatreche, Y. Li, and L. P. Maguire, "A supervised learning algorithm for learning precise timing of multiple spikes in multilayer spiking neural networks," *IEEE Transactions on Neural Networks and Learning Systems*, vol. 29, no. 11, pp. 5394–5407, 2018.
- [21] M. Zhang, J. Wang, J. Wu, A. Belatreche, B. Amornpaisannon, Z. Zhang, V. P. K. Miriyala, H. Qu, Y. Chua, T. E. Carlson, and H. Li, "Rectified linear postsynaptic potential function for backpropagation in deep spiking neural networks," *IEEE Transactions on Neural Networks and Learning Systems*, vol. 33, no. 5, pp. 1947–1958, 2022.
- [22] J.-P. Pfister, T. Toyozumi, D. Barber, and W. Gerstner, "Optimal spike-timing-dependent plasticity for precise action potential firing in supervised learning," *Neural Computation*, vol. 18, no. 6, pp. 1318–1348, 2006.
- [23] B. Gardner, I. Sporea, and A. Grüning, "Learning spatiotemporally encoded pattern transformations in structured spiking neural networks," *Neural Computation*, vol. 27, no. 12, pp. 2548–2586, 2015.
- [24] C. Ma, R. Yan, Z. Yu, and Q. Yu, "Deep spike learning with local classifiers," *IEEE Transactions on Cybernetics*, 2022.
- [25] Q. Zhan, G. Liu, X. Xie, G. Sun, and H. Tang, "Effective transfer learning algorithm in spiking neural networks," *IEEE Transactions on Cybernetics*, 2021.
- [26] Y. Li, S. Deng, X. Dong, R. Gong, and S. Gu, "A free lunch from ANN: Towards efficient, accurate spiking neural networks calibration," in *International Conference on Machine Learning*. PMLR, 2021, pp. 6316–6325.
- [27] J. Deng, W. Dong, R. Socher, L.-J. Li, K. Li, and L. Fei-Fei, "ImageNet: A large-scale hierarchical image database," in *2009 IEEE Conference on Computer Vision and Pattern Recognition*. Ieee, 2009, pp. 248–255.
- [28] J. Wu, Y. Chua, M. Zhang, G. Li, H. Li, and K. C. Tan, "A tandem learning rule for effective training and rapid inference of deep spiking neural networks," *IEEE Transactions on Neural Networks and Learning Systems*, 2021.
- [29] P. U. Diehl, D. Neil, J. Binas, M. Cook, S.-C. Liu, and M. Pfeiffer, "Fast-classifying, high-accuracy spiking deep networks through weight and threshold balancing," in *2015 International Joint Conference on Neural Networks (IJCNN)*. Ieee, 2015, pp. 1–8.
- [30] B. Rueckauer, I.-A. Lungu, Y. Hu, M. Pfeiffer, and S.-C. Liu, "Conversion of continuous-valued deep networks to efficient event-driven networks for image classification," *Frontiers in Neuroscience*, vol. 11, p. 682, 2017.
- [31] S. Deng and S. Gu, "Optimal conversion of conventional artificial neural networks to spiking neural networks," in *International Conference on Learning Representations*, 2021.
- [32] S. Kim, S. Park, B. Na, and S. Yoon, "Spiking-YOLO: Spiking neural network for energy-efficient object detection," in *Proceedings of the AAAI Conference on Artificial Intelligence*, vol. 34, no. 07, 2020, pp. 11 270–11 277.
- [33] W. Tan, D. Patel, and R. Kozma, "Strategy and benchmark for converting deep q-networks to event-driven spiking neural networks," in *Proceedings of the AAAI Conference on Artificial Intelligence*, vol. 35, no. 11, 2021, pp. 9816–9824.

- [34] Y. Luo, M. Xu, C. Yuan, X. Cao, L. Zhang, Y. Xu, T. Wang, and Q. Feng, "SiamSNN: Siamese spiking neural networks for energy-efficient object tracking," in *International Conference on Artificial Neural Networks*. Springer, 2021, pp. 182–194.
- [35] Y. Kim, Y. Venkatesha, and P. Panda, "PrivateSNN: Privacy-preserving spiking neural networks," in *Proceedings of the AAAI Conference on Artificial Intelligence*, vol. 36, no. 1, 2022, pp. 1192–1200.
- [36] Z. Yan, J. Zhou, and W.-F. Wong, "Near lossless transfer learning for spiking neural networks," in *Proceedings of the AAAI Conference on Artificial Intelligence*, vol. 35, no. 12, 2021, pp. 10 577–10 584.
- [37] T. Bu, W. Fang, J. Ding, P. Dai, Z. Yu, and T. Huang, "Optimal ANN-SNN conversion for high-accuracy and ultra-low-latency spiking neural networks," in *International Conference on Learning Representations*, 2022.
- [38] N.-D. Ho and I.-J. Chang, "TCL: an ANN-to-SNN conversion with trainable clipping layers," in *2021 58th ACM/IEEE Design Automation Conference (DAC)*. IEEE, 2021, pp. 793–798.
- [39] Y. Wang, M. Zhang, Y. Chen, and H. Qu, "Signed neuron with memory: Towards simple, accurate and high-efficient ANN-SNN conversion," in *International Joint Conference on Artificial Intelligence*, 2022.
- [40] Q. Yu, C. Ma, S. Song, G. Zhang, J. Dang, and K. C. Tan, "Constructing accurate and efficient deep spiking neural networks with double-threshold and augmented schemes," *IEEE Transactions on Neural Networks and Learning Systems*, vol. 33, no. 4, pp. 1714–1726, 2022.
- [41] Y. Li and Y. Zeng, "Efficient and accurate conversion of spiking neural network with burst spikes," *arXiv preprint arXiv:2204.13271*, 2022.
- [42] Y. Cao, Y. Chen, and D. Khosla, "Spiking deep convolutional neural networks for energy-efficient object recognition," *International Journal of Computer Vision*, vol. 113, no. 1, pp. 54–66, 2015.
- [43] A. Sengupta, Y. Ye, R. Wang, C. Liu, and K. Roy, "Going deeper in spiking neural networks: Vgg and residual architectures," *Frontiers in Neuroscience*, vol. 13, p. 95, 2019.
- [44] Y. Xu, H. Tang, J. Xing, and H. Li, "Spike trains encoding and threshold rescaling method for deep spiking neural networks," in *2017 IEEE Symposium Series on Computational Intelligence (SSCI)*. IEEE, 2017, pp. 1–6.
- [45] Y. Hu, H. Tang, and G. Pan, "Spiking deep residual networks," *IEEE Transactions on Neural Networks and Learning Systems*, vol. 34, no. 8, pp. 5200–5205, 2023.
- [46] J. Ding, Z. Yu, Y. Tian, and T. Huang, "Optimal ANN-SNN conversion for fast and accurate inference in deep spiking neural networks," in *IJCAI*, 2021.
- [47] Y. Wang, Y. Xu, R. Yan, and H. Tang, "Deep spiking neural networks with binary weights for object recognition," *IEEE Transactions on Cognitive and Developmental Systems*, vol. 13, no. 3, pp. 514–523, 2020.
- [48] T. Bu, J. Ding, Z. Yu, and T. Huang, "Optimized potential initialization for low-latency spiking neural networks," in *Proceedings of the AAAI Conference on Artificial Intelligence*, 2022.
- [49] C. Stöckl and W. Maass, "Optimized spiking neurons can classify images with high accuracy through temporal coding with two spikes," *Nature Machine Intelligence*, vol. 3, no. 3, pp. 230–238, 2021.
- [50] B. Han and K. Roy, "Deep spiking neural network: Energy efficiency through time based coding," in *European Conference on Computer Vision*. Springer, 2020, pp. 388–404.
- [51] S. Hwang, J. Chang, M.-H. Oh, K. K. Min, T. Jang, K. Park, J. Yu, J.-H. Lee, and B.-G. Park, "Low-latency spiking neural networks using pre-charged membrane potential and delayed evaluation," *Frontiers in Neuroscience*, vol. 15, p. 629000, 2021.
- [52] B. Jacob, S. Kligys, B. Chen, M. Zhu, M. Tang, A. Howard, H. Adam, and D. Kalenichenko, "Quantization and training of neural networks for efficient integer-arithmetic-only inference," in *Proceedings of the IEEE Conference on Computer Vision and Pattern Recognition*, 2018, pp. 2704–2713.
- [53] M. Nagel, M. Fournarakis, R. A. Amjad, Y. Bondarenko, M. Van Baalen, and T. Blankevoort, "A white paper on neural network quantization," *arXiv preprint arXiv:2106.08295*, 2021.
- [54] Y. Wu, L. Deng, G. Li, J. Zhu, Y. Xie, and L. Shi, "Direct training for spiking neural networks: Faster, larger, better," in *Proceedings of the AAAI Conference on Artificial Intelligence*, vol. 33, no. 01, 2019, pp. 1311–1318.
- [55] Y. Bengio, N. Léonard, and A. Courville, "Estimating or propagating gradients through stochastic neurons for conditional computation," *arXiv preprint arXiv:1308.3432*, 2013.
- [56] A. Fan, P. Stock, B. Graham, E. Grave, R. Gribonval, H. Jegou, and A. Joulin, "Training with quantization noise for extreme model compression," *arXiv preprint arXiv:2004.07320*, 2020.
- [57] T. DeVries and G. W. Taylor, "Improved regularization of convolutional neural networks with cutout," *arXiv preprint arXiv:1708.04552*, 2017.
- [58] E. D. Cubuk, B. Zoph, D. Mane, V. Vasudevan, and Q. V. Le, "AutoAugment: Learning augmentation strategies from data," in *Proceedings of the IEEE/CVF Conference on Computer Vision and Pattern Recognition*, 2019, pp. 113–123.
- [59] T. Zhang, S. Jia, X. Cheng, and B. Xu, "Tuning convolutional spiking neural network with biologically plausible reward propagation," *IEEE Transactions on Neural Networks and Learning Systems*, vol. 33, no. 12, pp. 7621–7631, 2022.
- [60] N. Rathi, G. Srinivasan, P. Panda, and K. Roy, "Enabling deep spiking neural networks with hybrid conversion and spike timing dependent backpropagation," *ICLR*, 2020.
- [61] N. Rathi and K. Roy, "DIET-SNN: A low-latency spiking neural network with direct input encoding and leakage and threshold optimization," *IEEE Transactions on Neural Networks and Learning Systems*, vol. 34, pp. 3174–3182, 2023.
- [62] H. Zheng, Y. Wu, L. Deng, Y. Hu, and G. Li, "Going deeper with directly-trained larger spiking neural networks," in *Proceedings of the AAAI Conference on Artificial Intelligence*, vol. 35, no. 12, 2021, pp. 11 062–11 070.
- [63] S. Han, J. Pool, J. Tran, and W. Dally, "Learning both weights and connections for efficient neural networks," *Advances in Neural Information Processing Systems*, vol. 28, 2015.
- [64] N. Qiao, H. Mostafa, F. Corradi, M. Osswald, F. Stefanini, D. Sumislawska, and G. Indiveri, "A reconfigurable on-line learning spiking neuromorphic processor comprising 256 neurons and 128k synapses," *Frontiers in Neuroscience*, vol. 9, p. 141, 2015.
- [65] S. Xie, R. Girshick, P. Dollár, Z. Tu, and K. He, "Aggregated residual transformations for deep neural networks," in *Proceedings of the IEEE Conference on Computer Vision and Pattern Recognition*, 2017, pp. 1492–1500.
- [66] M. Sandler, A. Howard, M. Zhu, A. Zhmoginov, and L.-C. Chen, "MobileNetV2: Inverted residuals and linear bottlenecks," in *Proceedings of the IEEE Conference on Computer Vision and Pattern Recognition*, 2018, pp. 4510–4520.